Appl Phys A (2010) 98: 625–633
DOI 10.1007/s00339-009-5456-z

Applied Physics A
Materials Science & Processing

Micro-focussed XAFS spectroscopy to study Ni-bearing precipitates in the metal of corroded Zircaloy-2

G. Kuri · C. Degueldre · J. Bertsch · S. Abolhassani

Received: 15 May 2009 / Accepted: 12 October 2009 / Published online: 4 November 2009

Abstract The present work concerns an investigation of the local atomic environment of Ni-containing secondary phase precipitates (SPP) present in the metal-part of Zircaloy-2 cladding tubes. An unirradiated Zircaloy-2 and two specimens irradiated in a commercial nuclear power plant are characterized using μ-focussed synchrotron radiation, and by x-ray absorption fine structure (XAFS) spectroscopy. The patterns of Ni K-edge XANES and EXAFS of SPP in unirradiated and irradiated cladding are found different. Considering the fact that Ni-bearing SPP in the unirradiated samples are mainly Zintl phase Zr_2(Fe, Ni) type, a detailed EXAFS analysis of near-neighbor Ni atoms has been made. The result of a curve fit for the first two shells shows that about 2 Ni(Fe) and 8 Zr atoms are coordinated at 2.68 and 2.77 Å, respectively, around a central Ni atom in the SPP. XANES data analysis provides total electronic density of states at the Fermi level of unirradiated Zr_2(Fe, Ni). At the Ni K-edge EXAFS spectra of irradiated SPP, however, only a single scattering peak is observed demonstrating the structural disorder introduced by the neutron irradiation. The coordination number of the Ni neighboring shells is reduced markedly due to the formation of point and extended defects in the damaged SPP lattice. Dissolution of Ni from the SPP is also evident from the data. The results of this study provide a further basis for the description of both crystallographic and electronic structures of intermetallic second-phase precipitates found in Zr-based alloys.

PACS 61.82.Bg · 61.80.Hg · 78.70.Dm

G. Kuri (✉) · C. Degueldre · J. Bertsch · S. Abolhassani
LNM, NES, Paul Scherrer Institute, 5232 Villigen PSI, Switzerland
e-mail: goutam.kuri@psi.ch
Fax: +41-56-3102203

1 Introduction

Zircaloy-2 is a zirconium-based alloy traditionally used as a cladding and core structure material in nuclear power plants [1, 2]. Its application is based on zirconium's inherent properties in a wide range such as excellent corrosion resistance, high melting point and toughness, low cross sections for thermal neutron absorption, and exceptional stability under irradiation conditions. The material contains also several alloying elements, e.g., 1.2–1.7% Sn, 0.05–0.15% Cr, 0.07–0.20% Fe, and 0.03–0.08% Ni (all in weight% with the balance in Zr) as required to improve the properties of zirconium for nuclear applications. The commercially used Zircaloy-2 product is commonly β-quenched in one or several of the process steps during their fabrications [3]. In this context, while Sn is known to remain mostly in solid solution in the zirconium matrix, the inherent solubility for the transition metals Cr, Fe, and Ni (which also stabilize the β-phase) is very low [4], and these form submicron-size secondary-phase particles or precipitates (SPP) together with zirconium. The intermetallic SPP found in Zircaloy-2 are Zr(Fe, Cr)$_2$ and Zr_2(Fe, Ni). The Laves phase Zr(Fe, Cr)$_2$ has a hexagonal-closed-packed (hcp) or face-centered cubic structure. The ratio of Fe to Cr depends on the alloy composition of the bulk and the final heat treatment, normal values of Fe/Cr are about 1–2. The Ni-bearing SPP are mainly Zintl phase Zr_2(Fe, Ni) type having a body-centered-tetragonal (bct) lattice structure. Under the in-service reactor operational conditions, Zircaloy-2 cladding behavior for water-side corrosion strongly depends on the alloy microstructure and SPP distribution. Therefore, a thorough knowledge of the crystallographic structure, chemical composition, and morphology of the SPP are of special interest, since they are closely related to the corrosion behavior, changes in mechanical and metallurgical

properties, and hydrogen uptake of Zircaloy under neutron irradiations [5, 6].

A large number of studies have been published on the evolution of precipitates during oxidation of the zirconium alloys [3, 7–13]. The microstructure of the alloys was predominantly observed by various analytical methods, e.g., conventional optical microscopy, transmitted light optical microscopy, scanning electron microscopy (SEM), and transmission electron microscopy (TEM). The types of precipitates in the alloys were identified by analyzing the selected area diffraction (SAD) pattern in TEM and the chemical composition from the energy dispersive X-ray spectroscopy (EDS). Such studies are mostly concerned with differences in the size and distribution of SPP, including the extent of lattice deformation, and the corresponding differences in microstructural developments in the Zr matrix. It has been observed that oxidation of precipitates is delayed compared to the zirconium matrix [14]. The effect of SPP on metallurgical properties and corrosion has been also reported [10]. The properties of these intermetallics under irradiation environment in reactor up to a high burn-up have been the subject of several investigations [15–19]. However, structural aspects concerning lattice defects and their preferential location in these intermetallic phases have never been investigated. Since the sizes of these SPP are very tiny, their study for determining crystallographic structures by TEM on ultrathin specimens is often quite difficult due to the matrix contribution on the EDS spectrum and on the corresponding electron diffraction patterns. SPP volume fractions in Zr alloys also are very small. Therefore, a good statistic can only be obtained in TEM analysis by performing many examinations which are quite time consuming. Thus, the use of synchrotron-based X-ray absorption fine structure (XAFS) spectroscopy technique is of utmost interest. The ability of XAFS, both extended X-ray absorption fine structure (EXAFS) and X-ray absorption near edge structure (XANES), to yield local structural information in an atomic scale has been well documented in the literature [20].

Recently, imaging of SPP in Zircaloy-2 has been carried out using nano-focussed X-ray synchrotron radiation [21]. This allowed detection of Fe and Cr rich metallic precipitates with a diameter of 20 nm or greater. The Ni rich phases were not detected due to both the experimental limitations and the lower Ni concentration (compared to Fe or Cr) in the alloy. From the XANES spectra recorded for selected SPP at Fe and Cr $L_{2,3}$ edges, it has been possible to estimate the chemical state of these impurities. From this study we were also able to demonstrate the possible lattice environment (*cubic* and *hexagonal*, respectively, for Fe and Cr atoms) within the intermetallics. However, only XANES data did not provide any detailed structural information from Fe- and Cr-containing SPP [21]. In this work, a corroded and unirradiated Zircaloy-2 was selected as a first case to study in detail the local atomic structure of Ni-bearing SPP located at the metal side of the material. For the analysis, both EXAFS and XANES techniques have been used. Apart form the site symmetry of the absorbing atom, XANES data provide additional information about the unoccupied electronic states of the material and description of Fermi level. To complement the previous information and understand the SPP behavior under irradiation environment, EXAFS spectroscopic results of local structure around Ni atoms obtained from two irradiated specimens are also presented and qualitatively discussed.

2 Experimental

2.1 Materials, irradiation, and TEM

The specimens investigated here are taken from a Zircaloy-2 cladding material used in a boiling water reactor,[1] from the unirradiated state up to a burn-up of 66.9 MWd/kgU. The material contains several alloying elements with a nominal composition of 1.34% Sn, 0.18% Fe, 0.11% Cr, and 0.05% Ni (all in weight%) with the balance in Zr. The manufacturing details, metallurgical characteristics, and evolution of microstructural features following various stages of neutron irradiation of these specimens can be found in one of our previous publications [22]. Three selected samples from this batch were collected for XAFS measurements, and their results are presented in this work. Details of the specimens are summarized in Table 1. The as-received unirradiated sample was furthermore studied using a TEM (200 kV JEOL2010) equipped with an energy dispersive spectrometer to reveal the SPP sizes and distributions.

2.2 XAFS and data analysis

X-ray absorption experiments were performed at the undulator beam line X05L of the Swiss Light Source (SLS), Paul Scherrer Institute, Switzerland. The storage ring operates at electron beam energy of 2.4 GeV with a maximum stored current of 400 mA. The beam line provides a microfocussed (1 µm × 1 µm) spot size on the sample in the energy range 5 to 20 keV, and radioactive specimens are allowed at this facility: these were indeed extremely important in the present work for carrying out the measurements. A fixed-exit Si(111) double-crystal Bragg monochromator cooled with liquid nitrogen was used for the energy selection, the estimated energy resolution being about $\Delta E/E < 0.02\%$ at the Ni K-edge. Due to the high dilution of the alloying elements, all XAFS measurements have been made in the fluorescence mode. The incident X-ray intensities were

[1] http://www.kkl.ch.

Table 1 Description of the three Zircaloy-2 cladding tube (before and after irradiation in the reactor) specimens analyzed in this study

Specimen identification	Number of cycles	Assembly burn-up (MWd/kgU)	Irradiation fluence (n/cm^2 for $E > 1.35$ MeV)
Unirradiated	–	–	–
Sample-IA	3	34.7	5.9×10^{21}
Sample-IB	6	66.9	14.2×10^{21}

measured by means of an ultrathin Si-diode. The specimens were held at room temperature, and the fluorescence excitation spectra at the Ni K-edge were collected with an energy dispersive solid-state 32-element Ge detector. The measurement geometry was 45° (angle of incidence), and the detector was placed perpendicular to the beam direction. Integrated Ni fluorescent signal was optimized by changing the beam spot position (with a (sub)micron precision) on the samples. Several spectra (scans) were collected from each sample to have a better ratio signal/noise. For calibrating the energy output of the monochromator, the K-edge excitation energy of 8333 eV measured from a hyperpure nickel metallic foil, was set equal to the maximum of the first derivative of the XANES data.

XAFS data processing and numerical analysis were performed using the computer program IFEFFIT.[2] Considering the measurements geometry, an appropriate correction has been applied to all the measured data for the self-absorption effect [23]. The first step in the data analysis was a background subtraction. This was done using a linear function in the pre-edge region and a spline fit above the absorption edge. The threshold position E_0 was determined from the maximum of the first derivative of an absorption curve. Background-removed EXAFS function $\chi(k)$ was extracted and normalized by the edge jump height. $\chi(k)$ was then multiplied by k^3 to emphasize the higher k region. Thereafter, k^3-weighted EXAFS was Fourier transformed (FT) into real space to obtain a radial distribution function (RDF) of the near-neighbors around the absorber atom. Transform termination effects were minimized by choosing an appropriate window range bounded by minima in $|\chi(k)|$ and using a Hanning window function that smoothed the ends of the region to zero.

In the next step, the extracted experimental EXAFS signals were best fitted to the well-known EXAFS equation [20] available within the IFEFFIT algorithm. The optimized structural parameters, namely coordination number N, interatomic distance R, Debye Waller (DW) factor σ^2, and ΔE_0 (a correction to E_0) were derived from the fits, taking into account both the many-electron effects and the vibrations of neighboring atoms around their equilibrium positions. Quality of the fits were judged by the EXAFS $\Re$-factor as defined in the IFEFFIT code, and the acceptable values are in the order of a few percent. Theoretical scattering functions (phases and amplitudes) for quantitative EXAFS fitting were generated by the FEFF code [24]. This theoretical approach describes the photoelectron final states by an ab initio curved-wave multiple-scattering calculation using an energy-dependent exchange-correlation for self-energy within a muffin-tin potential. In our analysis, final-state potentials at Ni K-edge were calculated using atomic clusters derived from the known atomic coordinates of Zintl phase Zr_2(Fe,Ni) structures as referred in [25, 26].

3 Results and discussion

3.1 Second-phase particles observation by TEM

The precipitates present in the metallic matrix of unirradiated Zircaloy-2 are mainly Zr(Fe,Cr)$_2$ and Zr_2(Fe,Ni) with Fe/Cr and Fe/Ni ratios, respectively, close to 0.9 and 1.7. These characteristics are in good agreement with those described in our previous TEM studies [22] for the same alloys. A typical TEM micrograph of this specimen and corresponding elemental EDS mapping for Ni, Fe, and Cr are shown in Fig. 1. It is straightforward to distinguish between Fe/Cr and Fe/Ni intermetallics by EDS mapping. Some of the course Fe/Ni SPP are encircled in the figure. The number of Fe/Cr containing precipitates can be found larger than that of Fe/Ni particles. The precipitates also exhibit a range of sizes between 50 and 250 nm in diameter. It was confirmed from SAD pattern that these intermetallic particles are not amorphous in nature. As alluded, investigations by TEM on the evolution of microstructure, size distribution, and dissolution of SPP under irradiation have been discussed in prior research [22]. However, TEM observations do not allow any quantitative conclusions concerning atomic structures within SPP. It is worth noting in Fig. 1 that Ni-bearing particles are spatially separated by more than 1 µm (an average value). Therefore, the structural information that is gathered using a micro-focussed beam spot in XAFS analysis provides average result from an isolated SPP present at the (sub)surface regions of the specimens and a couple of individual SPP perhaps located along the beam path. At the Ni K-edge energy and 45° incidence angle geometry, the estimated x-ray probing depth in Zircaloy-2 is about 8 µm.[3]

[2] http://cars9.uchicago.edu/ifeffit/feffit.html.

[3] http://henke.lbl.gov/optical_constants/atten2.html.

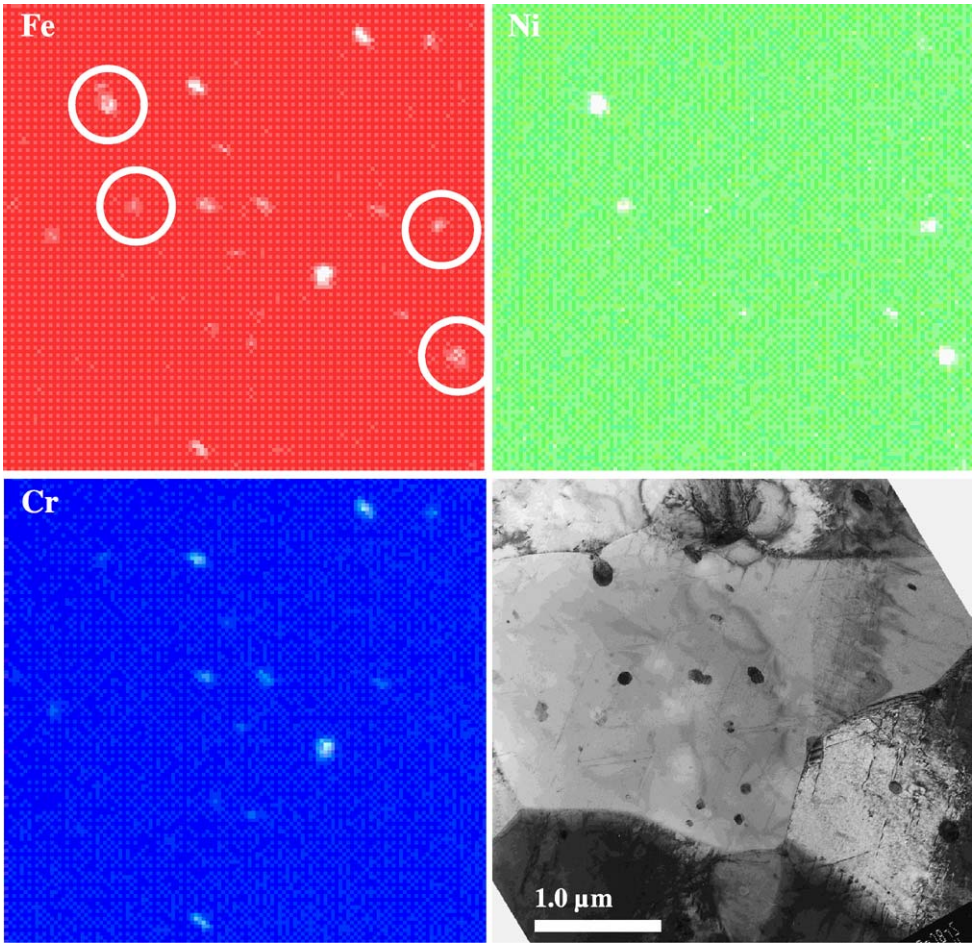

Fig. 1 Bright field TEM micrograph and EDS elemental maps of Fe, Ni, and Cr illustrating the size distribution of Ni–Fe and Fe–Cr bearing precipitates in the unirradiated Zircaloy-2 sample analyzed in this work

3.2 EXAFS and XANES on unirradiated material

The use of unirradiated Zircaloy-2 material is essential for interpretation of EXAFS results from irradiated specimens, as they provide directly comparable structural information. In this respect, a comprehensive quantitative analysis of the XAFS data measured from this pristine specimen has been made. The results are shown in Fig. 2. The upper panel in the figure reports representative Ni K-edge XAFS spectrum (Fig. 2a). The edge position, taken as equal to the maximum value of the differential coefficients of the spectrum near the edge, reveals an E_0 value of 8332 eV, which is 1 eV smaller than that of the Ni-metal foil (XANES spectrum shown later). For a quantitative analysis of this data, the fitting procedure was adopted using the standard methods as summarized in the experimental section. The resulting RDF is shown in Fig. 2a as an inset. The FT was performed in the spectral k range of 3–11 Å^{-1}. The spectra drawn with points and solid curves are the observed and corresponding best-fitted ones, respectively. The lower panel (Fig. 2b) plots the XANES part of the data (presented in Fig. 2a) as well as the spectrum derived from FEFF calculations.

The EXAFS measurement from pristine Zircaloy-2 clearly reveals an excellent crystallinity around Ni atoms. The FT data presented in Fig. 2b illustrates Fourier features which are characteristics of the *bct*-sites environments. The RDF shows that there are three strong amplitude peaks between 2 and 7 Å, where the distance R is around 2.8, 4.8, and 6.1 Å, respectively. A small structure peaking at about 3.7 Å can be also seen in the spectrum. The first strong peak at about 2.8 Å stems from the first and second neighbors (Ni and Zr atoms, respectively) of the Zr_2(Fe, Ni) lattice. The magnitude intensity of the second peak near 4.8 Å is sensitive to the complicated environment of Ni atoms consisting of 30 neighbors (both Ni (or Fe) and Zr) in five coordination shells. The bimodal peak around 6.1 Å contain contributions from long-range order (beyond the first seven shells).

The starting model employed to analyze these data was to use the C16-type crystal structure of Zr_2Ni with space-group symmetry D_{4h}^{18}-I_4/mcm (no 140). This structure is characterized by a Zr_2Ni unit cell, which is used in our calculations, contains four Zr atoms at the positions $(\frac{1}{2}-x, x, 0)$, $(1-x, \frac{1}{2}-x, 0)$, $(\frac{1}{2}+x, 1-x, 0)$, $(x, \frac{1}{2}+x, 0)$ and the Ni atoms at the positions $(0, 0, \frac{1}{4})$ and $(\frac{1}{2}, \frac{1}{2}, \frac{1}{4})$. Here x represents the atomic parameter [26]. For the lattice and atomic

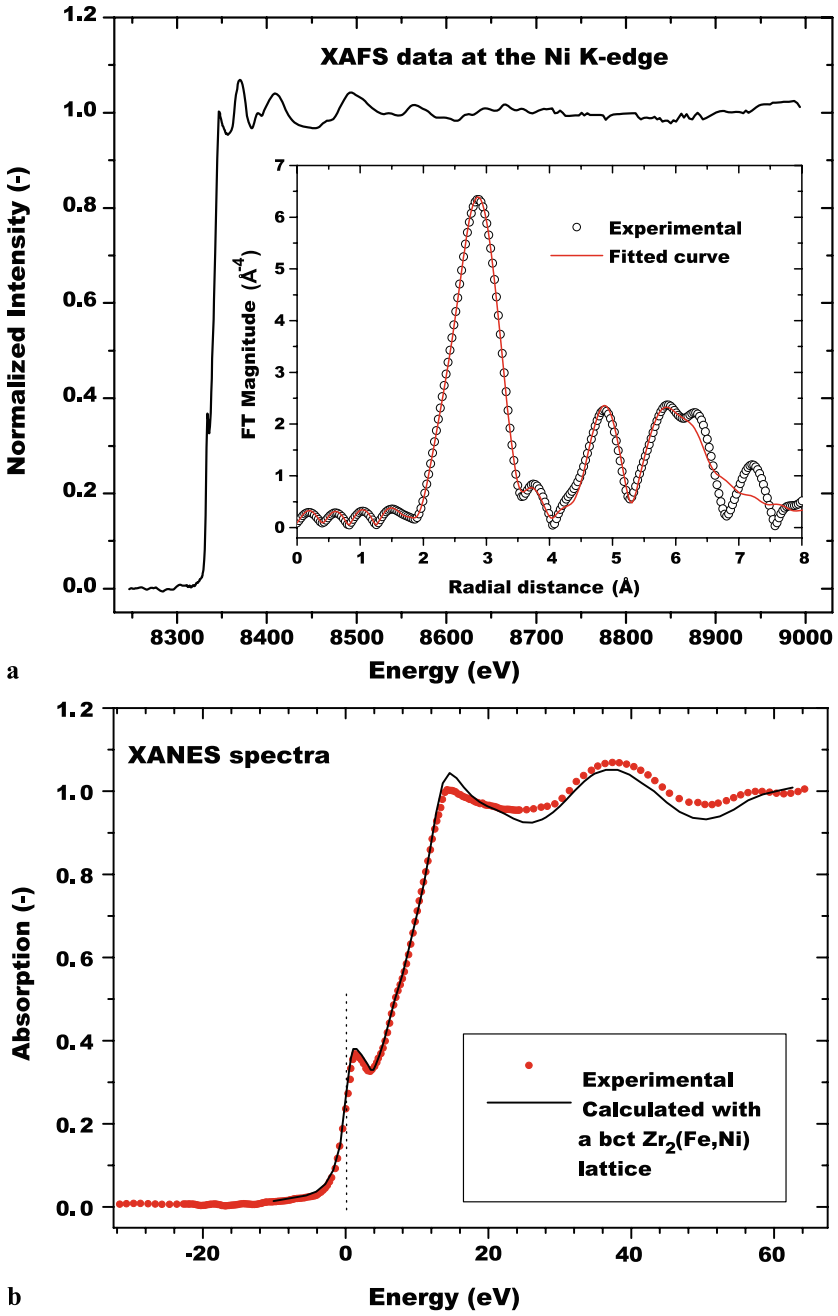

Fig. 2 (**a**) Normalized and background removed Ni K-edge XAFS spectrum for the unirradiated Zircaloy-2 sample measured with a μ-focussed X-ray beam. The inset shows magnitude of the associated Fourier transform of the experimental EXAFS signal. (**b**) Near-edge part of the experimental XAFS data shown in (**a**) and the simulated XANES spectrum at the Ni K-edge obtained from FEFF code. The theoretical calculation has been carried out using a *bct* lattice of Zr_2(Fe,Ni) structural model. See the text for further details

parameters, we have used $a = b = 6.431$ Å, $c = 5.418$ Å, and $x = 0.168$. These values have been calculated using the literature data [27] for unit cells of pseudo-binary alloys Zr_2Fe and Zr_2Ni, and taking into consideration the fact that average (atomic) ratio of Fe/Ni in the SPP yields a value of 1.45 ± 0.15 [22]. The crystallographic parameters for the first five shells are given in Table 2. Information about the local structure in this unirradiated sample is, thereafter, obtained by fitting experimental data with the corresponding atomic scattering functions calculated using FEFF [24] for a $Zr_2Fe_{0.6}Ni_{0.4}$ lattice with the crystallographic parameters just mentioned. The analysis resulted a good fit to the experimental data. The starting FEFF model comprises all single scattering paths within the fit range and all multiple scattering paths up to 6.0 Å. During the preliminary fitting analysis, the R, σ^2, and ΔE_0 of contributing atom shells were floated, while all other parameters were held fixed at their theoretical values. Once approximate values of the radial distances and DW factors were determined, additional fits were carried out in which the R and σ^2 values were fixed and the N, S_0^2, and ΔE_0 values were allowed to vary. Further refinement of the fit was achieved by fixing the N, S_0^2, and σ^2 values at the fitted values and again varying R using the previously determined values as the starting values. Finally, all parameters

Table 2 Crystallographic data of coordination numbers (N) and interatomic distances (R) in crystalline Zr_2Ni

Absorbing atom	Neighboring atom	N	R (Å)	Note
Ni	Ni	2	2.67	First five
	Zr	8	2.75	shells
	Ni	4	4.54	
	Zr	8	4.63	
	Zr	8	4.71	
Zr	Ni	4	2.75	15 atoms
	Zr	1	3.03	in five
	Zr	2	3.09	coordination
	Zr	4	3.38	shells
	Zr	4	3.46	

Table 3 Ni EXAFS fit parameters of the first two coordination shells

Specimen identification	SC	CN (±0.3)	RD (nm) (±0.002)	σ^2 (Å^2) (±15%)	Quality factor (R)
Un-irradiated	Ni–Ni	1.5	0.268	0.0091	0.013
Zircaloy-2	Ni–Zr	7.5	0.277	0.0145	

SC: scattering configuration; CN: coordination number; RD: radial distance

were floated from the starting values determined from the above approach until a best fit for all parameters was obtained. All data in Fig. 2 have also been corrected for electron phase shifts using the first shell-path from FEFF, and therefore the FT peaks should correspond directly with the true bond distances of the near neighbors. At this point let us mention that Ni and Fe atoms, when compared in terms of their sizes, behave as equivalent backscatterers and are indistinguishable from the XAFS point of view. Therefore, in our present analysis, the local environment of Ni atoms has been deduced assuming only two kinds of neighbors (Ni–Ni and Ni–Zr) for the central atom residing in a *bct* $Zr_2Ni(Fe)$ lattice. In this way the correlation among $R_{Ni–Ni}$, $R_{Ni–Fe}$, and ΔE_0 was reduced, and hence the number of free parameters in the fit. This approximation is reasonable, since Ni and Fe are similar in their ionic radii and have very close values of electronegativity [28]. Therefore, the electrostatic potentials induced by charge transfer between Ni and Fe atoms can be neglected, and the approximation of neutral absorber atom assumed by FEFF is valid, so that an overall R and ΔE_0 are enough for all scattering events. Thus, the contributions from Ni–Ni correlation (for example) in the FT peak (see Table 3) imply the results of Ni–Ni(Fe) atoms-shell in practice, Ni being the central atom.

Table 3 contains the analyzed numerical results for the first two coordination shells. The refined values obtained from the curve fit give realistic DW factors, correct order for the bonds, and appropriate coordinations for the next-neighbor shells. The total numbers of the Ni emitter for the first two shells are $N_{Ni–Ni} = 1.5 \pm 0.3$ and $N_{Ni–Zr} = 7.5 \pm 0.3$. These values are consistent with corresponding values reported by using X-ray crystallography [25] and XAFS studies on crystalline nickel–zirconium alloys [29]. The measured Ni–Ni bond distance is 2.68 ± 0.02 Å in the first coordination shell. Describing the $R_{Ni–Zr}$ result, we notice that the eight-fold Zr neighbors provide an average bond distance of 2.77 Å, which is significantly smaller than the sum of the elemental radii of constituting atoms (Ni, 1.35 Å; Zr, 1.55 Å[4,5]). This can be explained by a charge transfer from the Zr to the Ni atoms in the Zr_2Ni alloy. Such an explanation is in accordance with the Ni–Zr interaction which is indicated by the shortened bond length with respect to the pure Ni element, and a shift of 1 eV to a lower energy of the Ni-edge position (E_0 value) in the SPP analyzed. Further support for this conclusion can be obtained by the local density of states calculations of Zr_2Ni C16 compound [30]. A charge transfer from the Zr 4*d* orbitals to the unfilled Ni 3*d* shell leads to a decrease of the effective Zr radius. Concerning the DW factors, our results indicate σ^2 much larger for the Ni–Zr pair (145×10^{-4} Å^2) compared with Ni–Ni pair (91×10^{-4} Å^2). For comparing these values of DW factors with the existing literature, we have not come across any report of XAFS describing the Ni environment within SPP in Zircaloy-2. The available data of σ^2 reported in [29] for Ni–Ni and Ni–Zr pairs have been measured only at low temperatures (~77 K). Let us also note that Zr atoms are rather heavy scatterers and the Ni chains are relatively free to vibrate with respect to the Zr host lattice.

Ni K-edge experimental and calculated (using FEFF) XANES spectra of an unirradiated sample are shown in Fig. 2b. Because the Fermi energy of the experimental curve is not known absolutely, the first inflection points (marked by a dotted line in the plot) of the theoretical and experimental curves are approximately lined up and also normalized to each other. Features present in the XANES spectrum are dependent on both the local atomic arrangement around the photo absorber and the electronic states of constituent elements in the alloy. Furthermore, the near-edge range XANES of XAFS spectra give information about the unoccupied local density of states projected at atom sites (LDOS). The FEFF calculation itself is characterized by the following technical details. Muffin-tin exchange and correlation Hedin–Lundqvist potentials were used. Self consistency calculations were refined with a radius of 4.0 Å around the central Ni. For the full multiple-scattering calculations, we have chosen a radius of 7.2 Å to obtain about 100 atoms

[4] http://www.webelements.com/nickel/atom_sizes.html.

[5] http://www.webelements.com/zirconium/atom_sizes.html.

in the simulated cluster. The refined experimental parameters obtained from the EXAFS analysis were reintroduced in FEEF for calculation of the XANES and LDOS. Since the code was unable to reproduce the experimental XANES features during the preliminary analyses, several calculation parameters of the code were varied, aiming to analyze their influence on the theoretical spectra. After some tests, the final calculation comprised the use of a full multiple scattering method [31, 32], appropriate correction factors related to the Fermi level estimate (using EXCHANGE and CORRECTIONS cards in FEFF), and the Debye temperature of Zr_2Ni (252 K [33]) in DW factor calculations. A statistical structural disorder in the atomic layers was furthermore incorporated with the help of the SIG2 card (a value of 0.004) in FEFF. In this way it was possible to obtain a reasonable agreement between experiment and computed spectrum, in terms of both absolute magnitudes and the line-shape. Relative positions and intensities for the dominant XANES features present in the Ni-bearing SPP modeled are reproduced (see Fig. 2b).

Continuing the discussion on XANES results, for Zr_2Ni, we find a Fermi level (E_F) of -10.9 eV with our input option in LDOS calculations. In Fig. 3, we show the local partial electron densities of states (DOS) for Ni and Zr components and the total DOS for compound Zr_2Ni found from the analysis. It is clear that E_F lies at a valley in DOS for Zr_2Ni. The broad and three-humped pattern above Fermi level is arising predominantly from the heavier Zr atom, while the sharp peak around -2.5 eV in Fig. 3a is due to the lighter atom Ni. For the alloy, total electronic DOS at E_F is predominantly due to d-electrons on the Zr and Ni sites. Also, there is a nonzero contribution from p-DOS at the Fermi level, although in the atomic state both Zr and Ni atoms have only s- and d-electrons ($3d^8 4s^2$ for Ni; $4d^2 5s^2$ for Zr). These results are in qualitative agreement with the band model of C16 Zr_2M (M = Fe, Co, Ni, Rh) compounds [34, 35] and with the electronic structure calculation of Zr_2Ni using the tight-binding approximations [30]. Since the electron conduction mechanism of ZrO_2 involving intermetallic SPP is expected to be a band mechanism, the description of the electronic structure provided here is important for explaining the oxide growth resulting from oxygen migration through the oxide where the rate of oxidation is known to be controlled by either ionic or electronic conductivity of the oxide layer [5, 6].

3.3 XAFS on irradiated material

Dealing with neutron irradiated samples, the RDFs exhibit remarkable differences in many respects. Significant radiation damage effects are readily apparent in the raw data. Figure 4 displays the Ni K-edge XAFS spectra measured from the two irradiated samples, which is detailed

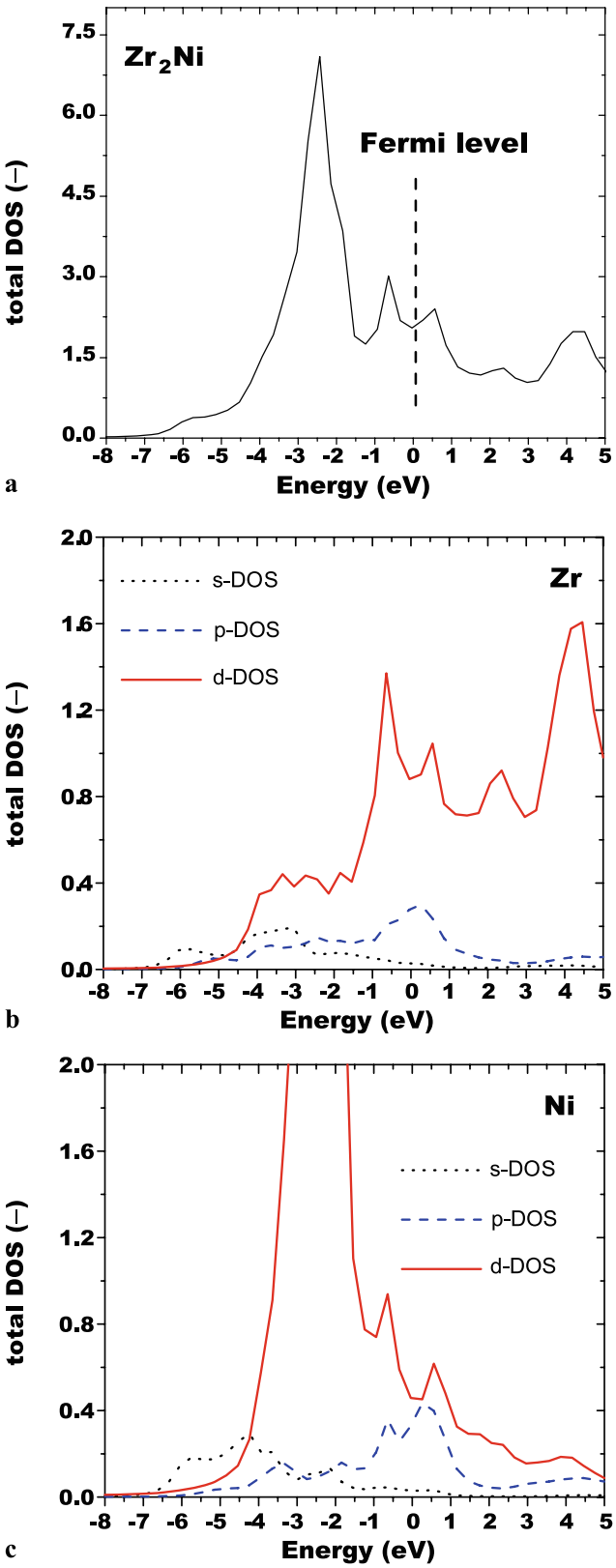

Fig. 3 (**a**) The total electronic density of states (DOS) for the alloy Zr_2Ni derived from the analysis. The angular momentum projected partial l-DOS for Zr (**b**) and Ni (**c**) in the compound Zr_2Ni are also shown

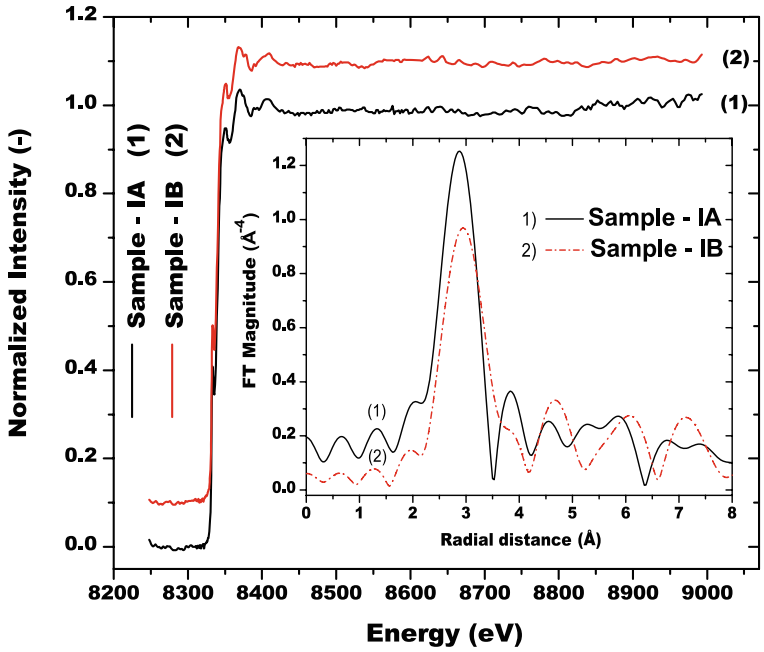

Fig. 4 Ni K-edge XAFS spectra and the corresponding Fourier transforms (*inset*) showing the experimental data for two neutron-irradiated samples as described in Table 1

in Table 1. A notable feature is the absence of any strong high-frequency contribution of experimental EXAFS signals from distant coordination shells; apparently, they are smeared out by a strong static disorder. In the interval 2 to 6.5 Å, RDFs (inset in Fig. 4) show only a major peak at about 3 Å and a nonzero contribution at about 4 Å with no significant signal above this value. These structures can be attributed to the first two coordination shells around Ni atoms and to multiple-scattering effects. Our preliminary analysis, however, has demonstrated that the multiple-scattering contribution is negligible and that the structures in the range 2.0–4.2 Å in Fig. 4 (inset) are predominantly due to the Ni–Zr pair correlation. The contribution from Ni–Ni pair is practically negligible from EXAFS perspective. Similar behavior was earlier observed in an x-ray scattering study performed on an amorphous Zr_2Ni alloy, in particular for the Ni–Ni pairs which have the smallest weighting factor [36]. Comparing the unirradiated and irradiated SPP, it is evident that a transformation towards a state of greater structural disorder has taken place upon irradiation, as manifested most notably by a reduction in the EXAFS amplitudes.

Although the XAFS spectra in Fig. 4 of two irradiated samples look rather similar, some definite differences can be seen from their FT data (inset in Fig. 4). A systematic attenuation experienced by the major FT-peaks is evident. The amplitude reduction is strongest for the specimen irradiated with the highest neutron fluence (sample IB). These results can be attributed to both the dissolution of SPP and the presence of strong structural disorder in intermetallic Ni-compounds, causing local deformations of bond distances and localization of different atomic sites in the amorphous network within the SPP. In the literature it is discussed that amorphization occurs because the irradiated crystalline structure gets unstable due to the accumulation of radiation damage [37, 38]. The irradiation-induced dissolution is due to the increase in the number of accumulated point defects (mostly vacancies) in the matrix and the increase in the solubility limits of Fe and Ni under neutron irradiation [39]. It has to be mentioned that XAFS results presented above for the irradiated SPP are only qualitative. The parameters (e.g., N, R, or σ^2) of the local structure around Ni in next-neighbor shells are not reported here not only because of the poor best-fit quality parameter ($\Re$) but also because of the instability of quantitative results obtained from the assumed initial lattice structure of $Zr_2Fe_{0.6}Ni_{0.4}$ for the FEFF calculation as applied for unirradiated SPP. A detail analysis of the damage state, e.g., point and extended type of defects including anti-site irregularities [40] in irradiated Zr_2(Fe, Ni) is underway.

4 Conclusions

X-ray absorption spectroscopy is a local probe and thus appears to be a good tool to study both crystallographic and electronic structures of submicron-size intermetallic secondary-phase precipitates (SPP) found in Zircaloy-2. In this study, μ-focussed XAFS spectroscopy has been used to investigate local structure around Ni atoms of intermetallic Zr_2(Fe, Ni) SPP located at the metal-side of corroded and irradiated Zircaloy-2 specimens. Characterization of SPP in the corrosion layer and/or at the metal/metal-oxide interface remains subject of future investigations after reactor service. Two selected cladding tube specimens from fuel rods

(see Table 1 for details) and one unirradiated specimen of the same material are collected for XAFS measurements. Fourier transformed (FT) Ni K-edge EXAFS spectrum of the unirradiated SPP exhibits several nearest-neighbor peaks indicating a good crystallinity around Ni atoms in the alloy. Long-range order (beyond the first- and second-shell) is readily apparent in the FT-spectrum. A detail curve fit analysis shows that the Ni-sites accommodate about 1.5 ± 0.3 Ni atoms and 7.5 ± 0.3 Zr atoms in the first two consecutive neighbor shells. The measured Ni–Ni and Ni–Zr bond distances are 2.68 ± 0.02 and 2.77 ± 0.02 Å, respectively. On the contrary, the FT-spectra of irradiated SPP are dominated by a single scattering peak. Results of preliminary analyses of EXAFS data from these irradiated material clearly show no coherent scattering contributions from beyond the Ni first neighbor shell, loss of Ni from the alloy, and a reduced coordination number in the Ni–Zr pair with some disruption of the average bond distances. These imply presence of strong structural disorder in intermetallic Ni-bearing SPP, causing local deformations of bond distances and localization of different atomic sites in the amorphous network within SPP. The local structure of intermetallic SPP is an important step to understand the irradiation effects including differences between damaged state and crystalline phase, and with respect to the corrosion behavior of the material. It is demonstrated that XAFS can be a powerful local probe towards these aspects.

Acknowledgements The authors gratefully acknowledge Hot-Laboratory technical-staff at PSI for preparing the radioactive specimens and μ-XAS beam-line staff for the experimental work performed at SLS. We also appreciate the useful scientific discussion with D. Gavillet. Our sincere thanks are to swissnuclear for financial supporting this work.

References

1. S.R. MacEwen, J. Faber, A.P.L. Turner, Acta Metall. **31**, 657 (1983)
2. P. Hofmann, J. Nucl. Mater. **270**, 194 (1999)
3. A.R. Massih, M. Dahlbäck, M. Limbäck, T. Andersson, B. Lehtinen, Corros. Sci. **48**, 1154 (2006)
4. D. Charquet, R. Hahn, E. Ortlieb, J.P. Gros, J.F. Wadier, Zirconium in the nuclear industry, ASTM STP, vol. 1023 (1988), p. 405
5. B. Cox, J. Nucl. Mater. **336**, 331 (2005)
6. A. Yilmazbayhan, A.T. Motta, R.J. Comstock, G.P. Sabol, B. Lai, Z. Cai, J. Nucl. Mater. **324**, 6 (2004)
7. D. Pecheur, F. Lefebvre, A.T. Motta, C. Lemaignan, D. Charquet, in: *Zirconium in the Nuclear Industry, Tenth International Symposium, ASTM STP*, vol. 1245, ed. by A.M. Garde, E.D. Bradley (1994), p. 687
8. J.H. Baek, Y.H. Jeong, J. Nucl. Mater. **304**, 107 (2002)
9. M.Y. Yao, B.X. Zhou, Q. Li, W.Q. Liu, Y.L. Chu, J. Nucl. Mater. **350**, 195 (2006)
10. S.A. Nikulin, V.I. Goncharov, V.A. Markelov, V.N. Shishov, Zirconium in the Nuclear Industry, Eleventh Symposium, ASTM STP, vol. 1295 (1996), p. 695
11. H.-G. Kim, J.-Y. Park, Y.-H. Jeong, J. Nucl. Mater. **345**, 1 (2005)
12. J.-Y. Park, S. Jo Yoo, B.-K. Choi, Y.H. Jeong, J. Nucl. Mater. **373**, 343 (2008)
13. R. Benaboud, P. Bouvier, J.-P. Petit, Y. Wouters, A. Galerie, J. Nucl. Mater. **360**, 151 (2007)
14. Y. Hatano, M. Sugisaki, K. Kitano, M. Hayashi, Zirconium in the Nuclear Industry, Twelfth International Symposium, ASTM STP, vol. 1354 (2000), p. 901; and references therein
15. A.T. Motta, J. Nucl. Mater. **244**, 227 (1997)
16. S. Shimada, Y. Etoh, K. Tomida, J. Nucl. Mater. **248**, 275 (1997)
17. P. Vizcaino, A.D. Banchik, J.P. Abriata, Mater. Lett. **62**, 491 (2008); and references therein
18. C. Rodriguez, D.A. Barbiric, M.E. Pepe, J.A. Kovacs, J.A. Alonso, R.H. de Tendler, Intermetallics **10**, 205 (2002); and references therein
19. P. Vizcaino, A.D. Banchik, J.P. Abriata, J. Nucl. Mater. **336**, 54 (2005)
20. P.A. Lee, P.H. Citrin, P. Eisenberger, B.M. Kincaid, Rev. Mod. Phys. **53**, 769 (1981)
21. C. Degueldre, J. Raabe, G. Kuri, S. Abolhassani, Talanta **75**, 402 (2008)
22. S. Abolhassani, D. Gavillet, F. Groeschel, P. Jourdain, H.U. Zwicky, in: International Topic Meeting on LWR Fuel Performance, Park City, UT, April 10–13 (2000), p. 470
23. C.H. Booth, F. Bridges, Phys. Scr. T **115**, 202 (2005)
24. J.J. Rehr, J.M.d. Leon, S.I. Zabinsky, R.C. Albers, J. Am. Chem. Soc. **113**, 5135 (1991); we have used the version 8.20
25. M.E. Kirkpatrick, D.M. Bailey, J.F. Smith, Acta Cryst. **15**, 252 (1962)
26. E.E. Havinga, H. Damsma, P. Hokkelling, J. Less-Common Met. **27**, 169 (1972)
27. National Institute of Standards and Technology; NIST/FIZ FindIt-code for Inorganic Crystal Structure Database (ICSD); We have used ICSD # 103712 and ICSD # 105479 for Zr_2Fe and Zr_2Ni, respectively
28. J.A. Alonso, L.A. Girifalco, Phys. Rev. B **19**, 3889 (1979)
29. R. Frahm, R. Haensel, P. Rabe, J. Phys. F: Met. Phys. **14**, 1029 (1984)
30. R. Visnov, F. Ducastelle, G. Treglia, J. Phys. F: Met. Phys. **12**, 441 (1982)
31. A.L. Ankudinov, B. Ravel, J.J. Rehr, S.D. Conradson, Phys. Rev. B **58**, 7565 (1998)
32. A.L. Ankudinov, J.J. Rehr, Phys. Rev. B **62**, 2437 (2000)
33. R. Mittal, S.L. Chaplot, K.R. Rao, P. Raj, Physica B **222**, 233 (1996); and references therein
34. H.G. Salunke, G.P. Das, P. Raj, V.C. Sahani, S.K. Dhar, Physica C **226**, 385 (1994)
35. R. Mittal, S.L. Chaplot, H.G. Salunke, G.P. Das, P. Raj, A. Sathyamoorthy, K. Shashikala, S.K. Dhar, Physica C **320**, 239 (1999)
36. J.C. de Lima, D. Raoux, J.M. Tonnerre, D. Udron, K.D. Machado, T.A. Grandi, C.E.M. de Campos, T.I. Morrison, Phys. Rev. B **67**, 094210 (2003)
37. A.T. Motta, C. Lemaignan, in *Ordering and Disordering in Alloys*, ed. by A.R. Yavari (Elsevier Applied Science, London, 1992), p. 255
38. A.T. Motta, C. Lemaignan, J. Nucl. Mater. **195**, 277 (1992)
39. Y. Etoh, S. Shimada, J. Nucl. Mater. **200**, 59 (1993)
40. C.S. Moura, A.T. Motta, N.Q. Lam, L. Amaral, Nucl. Instrum. Methods Phys. Res. B **175–177**, 526 (2001)